Nonholonomic Modeling of Needle Steering

Robert J. Webster III
Jin Seob Kim
Noah J. Cowan
Gregory S. Chirikjian
Allison M. Okamura

Department of Mechanical Engineering
The Johns Hopkins University
{robert.webster,jkim115,ncowan,aokamura,gregc}@jhu.edu
http://www.me.jhu.edu/

Abstract

As a flexible needle with a bevel tip is pushed through soft tissue, the asymmetry of the tip causes the needle to bend. We propose that, by using nonholonomic kinematics, control, and path planning, an appropriately designed needle can be steered through tissue to reach a specified 3D target. Such steering capability could enhance targeting accuracy and may improve outcomes for percutaneous therapies, facilitate research on therapy effectiveness, and eventually enable new minimally invasive techniques. In this paper, we consider a first step toward active needle steering: design and experimental validation of a nonholonomic model for steering flexible needles with bevel tips. The model generalizes the standard three degree-of-freedom (DOF) nonholonomic unicycle and bicycle models to 6 DOF using Lie group theory. Model parameters are fit using experimental data, acquired via a robotic device designed for the specific purpose of inserting and steering a flexible needle. The experiments quantitatively validate the bevel-tip needle steering model, enabling future research in flexible needle path planning, control, and simulation.

KEY WORDS—nonholonomic system, steerable needle, surgical robot, medical robot, path planning, Lie group, Lie algebra

1. Introduction

Needle insertion is perhaps the most widespread surgical technique in existence. It is a critical aspect of many medical diagnoses, treatments, and scientific studies, including percutaneous procedures requiring therapy delivery to, or sample removal from, a specific location. However, errors in needle targeting can mitigate the effectiveness of diagnosis and therapy, or bias the results of scientific studies dependent on accurate needle placement. Without control and steering of the needle *inside* tissue, such targeting errors cannot be corrected, even though they often can be visualized. While needle-steering techniques are applicable to nearly all needle insertion procedures, the prostate, liver, and brain provide specific examples of organs where treatments might be improved by steerable needles. The goal of our research is to harness natural bending forces arising from the standard asymmetric bevel tip, creating new methods for accurate, dexterous targeting in percutaneous therapies, and steering needles under closed-loop control guided by medical imaging systems.

An accurate kinematic model of needle-tissue interaction is an essential first step toward closed-loop needle control to compensate for targeting and entry-angle error, as well as tissue deformation. This paper describes a needle-steering model, a robotic needle-steering system, and a set of experiments used to fit and validate the model. This work enables ongoing and future research in needle steering, including improved targeting for many percutaneous therapies and diagnostic methods, needle path planning to steer around obstacles, and realistic simulators for physician training and patient-specific planning. Steerable needles have the potential to enable entirely new minimally invasive surgical procedures by allowing needles to reach previously inaccessible locations in the body.

There are significant engineering challenges associated with generating steering capability in needles, stemming from the very small size of the needle, the required working channel through its center, and the diversity and inhomogeneity of tissues in which needles are used. Despite these challenges, several mechanisms have recently been proposed to enable needle steering within tissue. In the remainder of this section, we first motivate needle steering with three promising application areas, then describe the bevel-tip steering mechanism, and finally describe recent work on alternate mechanisms, comparing and contrasting them to bevel steering.

The International Journal of Robotics Research
Vol. 25, No. 5–6, May–June 2006, pp. 509-525
DOI: 10.1177/0278364906065388

Figures appear in color online: http://ijr.sagepub.com

1.1. Medical Motivation for Steerable Needles

Needles are used clinically in nearly every area of the body, and are one of the least invasive mechanisms for surgical treatment. Three compelling initial application areas for needle steering include the prostate, liver, and brain; these examples illustrate ways in which needle steering might address difficulties observed by surgeons using traditional straight, rigid needles, thereby improving targeting, enabling novel treatment methods, or reducing complication rates.

Prostate. Needle biopsy for diagnosis of prostate cancer is performed on about 1.5 million men per year and one in six men in the United States will be diagnosed with this condition at some time in their lives (Jemal 2004). A common treatment option is transperineal brachytherapy (Blasko et al. 2002), involving implantation of thin needles to deposit radioactive seeds (Cooperberg et al. 2004). In these procedures, it is challenging to achieve precise targeting in the event of organ dislocation and deformation. Significant seed-placement error can occur if the needle is tangential to the prostate capsule wall upon penetration (Wallner, Blasko, and Dattoli 2001). Hence, the ability to steer the needle and bevel to an optimal capsular penetration angle is of particular importance. After penetration, steering within the prostate may be useful for correcting the combined effects of deflection, dislocation, and deformation of the organ observed (but difficult or impossible to correct) in contemporary practice.

Liver. Hepatocellular (liver) cancer is one of the most common cancers in the world, and also one of the deadliest. Without treatment, the five-year survival rate is less than 5%, and the incidence is rising (Ulmer 2000). The liver is also the most frequent location of secondary tumors metastasized from colorectal cancer, with about 130,000 new cases and 60,000 deaths annually in the United States alone (Nakakura and Choti 2000). Liver tumors smaller than 5–6 cm in diameter are often treated with thermal ablation administered at the tip of a needle inserted through the skin and visualized using ultrasound. Since liver tumors often have very different mechanical properties than the surrounding tissue, they can behave as if encapsulated with respect to needle penetration, presenting challenges similar to those of the prostate. Also, "all but the smallest [liver] tumors" (Mulier et al. 2003) are large enough to require multiple overlapping thermal treatments for full coverage. Currently each treatment requires removing and re-inserting the needle. If it were possible to partially retract, steer, and redeploy the needle into an adjacent treatment zone, some targeting uncertainty and additional puncture wounds might be avoided.

Brain. In brain tissue, steerable needles might be used to stop the flow of blood from an intracranial hemorrhage (ICH), and remove resulting clots via targeted drug injection. The incidence of ICH ranges from 10 to 20 persons per 100,000, and untreated clot resolution takes two to three weeks, with an exceedingly high mortality rate of 50–75%. It is suggested that ultra-early intervention, given within three to four hours of onset, may arrest ongoing bleeding and minimize swelling of the brain after ICH (Mayer 2003). Precisely steered delivery vehicles have the potential to increase drug-target interactions and may enable very rapid removal of clots. In a typical emergency setting, a burr hole to introduce a device for injecting such drugs is drilled freehand and is seldom aligned with the optimal path to the target (as an emergency procedure, this surgery is not generally done by highly trained specialists). The location and orientation of the burr hole is fully dependent on the surgeon's hand-eye coordination, and the trajectory may be off-angle by as much 20–25 degrees. To compensate, the burr hole is usually made significantly larger than the diameter of the interventional tool, and this can lead to subsequent technical and clinical complications. Steerable devices may allow this hole to be much smaller, since steering can compensate for initial alignment error.

1.2. Bevel Steering Mechanism and Model Intuition

Physicians who have performed needle insertion know that needles with standard bevel tips (the most inexpensive and common tip design) can bend as they are inserted due to tip asymmetry. The angle of the bevel generates forces at the needle-tissue interface that causes the needle to bend as it is pushed into the tissue. While such bending is reduced in clinical practice by making the needle shaft as stiff as possible (usually out of stainless steel), the bevel (along with many other factors) can still cause clinically significant placement error. Some physicians have learned to exploit such bevel induced "error" to combat other sources of error by steering the needle using a combination of translation (insertion) and axial shaft rotation. However, this approach requires excellent 3D spatial reasoning, extensive experience, and high-resolution real-time image feedback, and the amount of bending achievable is severely limited by the high stiffness of the steel needle shaft.

In Webster et al. (2006), and this work, we enhance and magnify the bevel steering effect by making the shaft of the needle more flexible. We then use a robot to actuate the input degrees of freedom of the needle. With suitable model-based control techniques, a robot will be able to drive the needle tip to a desired target or along a desired path. To facilitate this, we wish to express the shape the needle will take in terms of the input degrees of freedom.

We hypothesize that a bevel tip needle can be modeled as a nonholonomic system with a steering constraint. There are clearly directions in which the tip may not instantaneously move when embedded in tissue. Similarly, the wheels of a bicycle or unicycle cannot instantaneously move sideways, despite their ability to attain any desired pose in the plane through a more complex sequence of motions. This is intuitively analogous to retracting the needle a certain distance, re-orienting the bevel tip, and then pushing it forward again

to achieve motion in a direction that would have been instantaneously impossible. Thus, we consider the needle to be a nonholonomic system, that is to say, one with nonintegrable velocity constraints (Murray, Li, and Sastry 1994). Such systems are path dependent, so determining the necessary set of inputs to reach a desired final configuration is not necessarily straightforward. However, nonholonomic motion planning and control have been studied extensively in the robotics and control literature, allowing us to draw upon a large body of work in the application of our model. Within this framework, it can be shown that judiciously chosen actuator input profiles will drive the needle along paths that allow it to reach difficult targets in locations potentially inaccessible via straight trajectories.

1.3. Related Work

Early work in needle modeling and simulation involved recording the forces applied to a needle during insertion and playing back "haptic recordings" or simple force versus position models in a force-feedback virtual environment (Hiemenz et al. 1996; Brett et al. 1997; Gorman et al. 2000). More recent work has modeled both tissue deformation and needle-tissue interaction forces. The geometry of the soft tissue for modeling and simulation purposes is now typically defined using a mesh composed of 2D or 3D polyhedral elements (Gibson and Mirtich 1997). The simulated forces exerted by the needle are used to compute deformations of the soft tissue mesh. Most past work using this approach has approximated the needle as infinitely thin and rigid (Alterovitz et al. 2003a; DiMaio and Salcudean 2003a), although some researchers have modeled needle geometry (thickness) and its effect on friction (Nienhuys and van der Stappen 2004).

Simulating needle insertion for medical procedures typically requires as input the properties of the needle and the soft tissue in which the needle will be inserted. DiMaio and Salcudean performed pioneering work in measuring and simulating the deformations that occur during needle insertion (DiMaio and Salcudean 2003a). A robot instrumented with a force sensor inserted a needle into 2D gel and deformations were captured with video and image processing. Using a quasi-static finite element method based on the acquired material parameters, they simulate the insertion of a rigid needle. Alterovitz et al. (2003a) proposed an alternative dynamic 2D model based on a reduced set of scalar parameters such as needle friction, sharpness, and velocity. For a given kind of surgery, such as prostate brachytherapy, this allows the needle designer to choose optimal parameter values (within limits) to improve needle placement accuracy. This model allows the authors to produce an interactive simulation and analyze the sensitivity of current medical methods to these parameters. In both of the simulators described above, the models considered only symmetric needle tips. Other researchers (Nienhuys and van der Stappen 2001; Mahvash and Hayward 2002) have been studying ways to integrate cutting into simulations. Their work has not addressed cutting by needle tips through experiments or complete simulations.

Setting accurate parameters for tissue properties is important for realistic needle insertion modeling in deformable tissues. Krouskop et al. (1998) estimated the elastic modulus for prostate and breast tissue using ultrasonic imaging. Kataoka et al. (2002) separately measured tip and frictional forces during needle insertion into a canine prostate, which is useful for simulation validation. Okamura, Simone, and O'Leary (2004) measured the stiffness, cutting and friction forces occurring during needle insertion into a bovine liver. Tissue properties can also be taken from handbooks (Fung 1993; Hayashi, Abe, and Sato 1996), or measured during procedures (Yen, Hibberd, and Davies 1996; Brett, Harrison, and Thomas 2000). Unknown parameters for needle insertion in some simulators, e.g. Alterovitz et al. (2003a,b,c), were set so that the output closely resembles an ultrasound video of a physician performing prostate brachytherapy on a patient.

The effects of needle bending have been explored by several groups. O'Leary et al. (2003) demonstrated experimentally that needle bending forces are significantly affected by the presence of a bevel tip, but did not generate a model for this behavior. Kataoka et al. (2001) attempted to create a model for needle deflection, but did not account for the bevel tip and admit that the bevel is likely to be the main source of deflection. DiMaio and Salcudean (2003b) and Glozman and Shoham (2004) have created finite element-type models for needle bending; their application to steering is described in more detail below.

Needle bending can also be generated using different strategies, such as incorporating a prebent stylus inside a straight cannula as is done by Okazawa et al. (2005). However, this method requires that the cannula be stiff relative to the stylus, and that the tissue, in turn, be stiff relative to the cannula, limiting the maximum curvature that the device can attain. Moreover, it is not clear if it is possible to change the direction of bending (e.g., "S" or "corkscrew" shapes) during a single insertion. Okazawa et al. also note that they have not yet addressed the 3D kinematics and planning problems, focusing their efforts on planar inverse kinematic planning using a single bend of the needle. Another similar prebent element design is a telescoping double cannula where the internal cannula is pre-bent (Daum 2003).

In order to steer a very flexible bevel tip needle, we have developed a specialized needle insertion robot. Thus, we provide here a brief review of robot-assisted percutaneous therapy. The idea of using robotic systems to insert needles is not new; many researchers have demonstrated improved targeting by utilizing the inherent stability, accuracy, and registration abilities of robots. A robot is better able than a human to translate information from medical images to 3D physical locations, and then to precisely align a needle to a target (Stoianovici, Webster, and Kavoussi 2005). Early work

on robot-assisted percutaneous therapy was done by Potamianos et al. (1994) who developed a robotic system for percutaneous renal access. Since 1995, the remote center of motion (RCM) concept has subsequently been used widely to align needles *outside* the body (Taylor et al. 1995a,b). Stoianovici et al. (2001) developed a chain-drive RCM robot that has been used for a variety of surgical procedures in conjunction with a radiolucent needle driver for percutaneous access. Many other researchers have also used robots for needle placement, including: Koyama et al. (1990); Masamune et al. (1995, 2001); Kaiser et al. (2000); Cleary et al. (2001); Yanof et al. (2001); Blasko et al. (2002).

These systems generally seek to increase the accuracy of the initial alignment of the needle (prior to insertion) as a means of reducing final targeting error. However, they do not address one of the most important factors contributing to targeting error, needle bending after insertion. None of the systems described above is able to offer accurate control of the needle path after entry into the body. A steerable needle will be less dependent on perfect initial alignment, allowing accurate targeting without requiring precise robots to perform perfect pre-entry alignment. Reducing precision necessary in the alignment mechanism will also reduce the cost of such systems, making them more readily available to hospitals, as was the goal of Boctor et al. (2005). We note that the idea of actively steering a surgical tool after insertion into the body has received interest in catheterization, where designs using shape memory alloys (Lim et al. 1996; Haga, Tanahashi, and Esashi 1998), as well as electro-active polymeric actuation (Guo et al. 1996) have been proposed. However, these systems are more complex and expensive than needles, and are not typically designed to cut through tissue.

There are only two recent studies that have analyzed robotic needle steering using bending and path planning. DiMaio and Salcudean (2003b) formulate a needle Jacobian that describes tip motion due to needle base motion and a tissue finite element model. Their needle is stiff relative to the tissue, and steering is accomplished by pulling on and angling the needle shaft outside the body to cause the tissue to deform. Our approach contrasts with theirs in that we consider a system where the needle is very flexible relative to the tissue, and does not displace a large amount of tissue in order to steer itself. Glozman and Shoham (2004) use an approach similar to DiMaio and Salcudean, but suggest a simplified model that allows fast path planning and real-time tracking for needle insertion procedures. Experiments in phantom tissues validate the accuracy of their model. Neither of the studies above consider the effect of tip asymmetry on steering, and both use standard stainless steel surgical needles, which are less flexible than the nitinol needles considered in our work.

The above method of steering via deforming tissue with a traditional stiff needle appears able to generate a large steering capability at shallow depths, but this ability degrades as depth increases (Glozman and Shoham 2004). More tissue must be deformed to generate steering, and more force must be applied to the tissue. Since there is clearly a safety limit on the maximum force that can be applied without tissue damage, there will be a corresponding depth where it is no longer possible to steer using this method. In contrast, while bevel steering and prebent element methods may generate somewhat less steering at shallow depths (no study exists comparing such steering amounts), their steering ability does not degrade with depth, and they do not require large force application or tissue deformation to achieve steering. Ultimately, we expect that a combination of force application at the needle base (the DiMaio and Glozman method) and our bevel steering techniques will be most accurate in describing and controlling needle insertions into human soft tissues.

To fully model or simulate needle steering in soft tissues, it is necessary to model the effect of cutting with a bevel tip and needle bending in 3D. All current models we are aware of either approximate the needle as a rigid object, restrict the motion of the needle to a 2D plane, or do not consider the effect of a bevel tip. These approximations may not be valid when the needle is very thin and flexible, as is the case in our specific needle steering system design, as well as in many medical procedures that seek to minimize tissue damage. Although the work described in this paper does not explicitly consider soft tissue deformation (since our system uses a needle that is much more flexible than the surrounding tissue by design), our model can be integrated with simulators handling deformation (Alterovitz, Goldberg, and Okamura 2005a), as is described in the Discussion section.

2. A Model for Bevel Tip Needle Steering

Consider a bevel-tip needle driven with two velocity inputs, insertion speed and rotation speed, actuated from the base of the needle. As the needle is inserted into tissue, the tissue imposes a reaction force on the bevel that deflects the needle tip, causing it to follow an arc. The rotational input at the base causes the needle to turn about its shaft reorienting the bevel. Neglecting the torsional compliance of the needle and assuming that the needle "stays in place" during reorientation, the tip rotates at the same speed as the base.

We model insertion speed and rotation speed as inputs to a kinematic nonholonomic system. We propose a variant of the standard kinematic bicycle, with constant front wheel angle, ϕ, and wheel base, ℓ_1, as depicted in Figure 1. Together ϕ and ℓ_1 specify the curvature, κ, of the needle path, and a second parameter, ℓ_2, determines the location along the bicycle that is attached to the needle tip, n. Roughly speaking, inserting the needle at speed u_1 is like "riding the bicycle" along a circular arc of radius $1/\kappa$ while rotating the needle at speed u_2 reorients the plane containing the bicycle's path. The two-parameter bicycle model can be reduced to a one-parameter "unicycle"

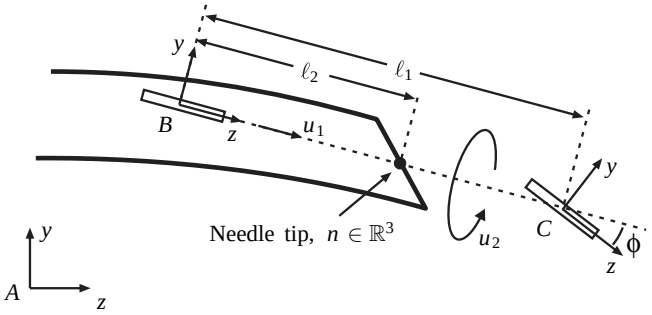

Fig. 1. Configuration of a bevel tip needle during steering showing the front and back "wheels" at frames B and C of a superimposed bicycle-like nonholonomic model. In this particular configuration, the x-axes for all three frames are pointing into the page.

model (a single wheel located directly at the needle tip) by appropriate simplifications that remove ℓ_2 while retaining κ.

The purpose of this study is to determine if the 3D generalizations of the standard nonholonomic bicycle and unicycle models quantitatively capture the needle steering kinematics. To do so, we fit the model parameters experimentally as described in Section 3. We then statistically compare the bicycle and unicycle models to determine if the additional bicycle model parameter significantly improves the model fit. We suspect that the model parameters depend on many factors such as tissue stiffness, needle stiffness, and bevel angle, but we leave verification of these hypotheses for future investigation, and reserve further speculation for Section 5.

2.1. Planar Needle Kinematics

If the material properties of the needle are appropriately selected with respect to the properties of the tissue through which it travels, the needle shaft follows the trajectory of the tip almost exactly. This was demonstrated in Webster, Memisevic, and Okamura (2005). using video of the needle insertion and comparing tip position in each frame to the final shaft trajectory (Figure 2). Thus, for an accurate representation of the entire needle shape, it suffices to describe the motion of the tip.

In the plane, the standard nonholonomic model for a single wheel or "unicycle" (Murray, Li, and Sastry 1994, Example 7.4) has a single no-slip constraint. As shown in Figure 3, when written in body frame coordinates this constraint is $v_y = 0$. In the standard unicycle model, the angular velocity ω is variable and serves as a control input to the system. However, the needle bevel tip angle is fixed. To model this, we can modify the standard unicycle model slightly by fixing the ratio of linear velocity to angular velocity. This constraint can be written (again in body frame coordinates) as $v_z = r\omega = \frac{1}{\kappa}\omega$, and causes the unicycle to trace out a circular path with radius r and curvature κ.

Similarly, the standard nonholonomic car or "bicycle model" (Murray, Li, and Sastry 1994, Example 7.5) can be modified slightly by fixing the angle of the front wheel. The two wheel constraints cause the bicycle to rotate as a rigid body about the point where the perpendicular axes intersect. If the needle tip was attached to the back wheel, this modified bicycle model would predict paths identical to the modified unicycle model for $\kappa = \frac{\tan\phi}{\ell_1}$. However, if we allow the needle attachment position to be at a distance ℓ_2 from the rear wheel, we add a parameter to the model.

If the needle path is simply a single circular arc, this new parameter does not add descriptive power. However, for any trajectory more complex than a single circle, its predicted shape will differ from the single parameter unicycle model. The utility of this will be illustrated in Section 3, where the model is fit to experimental data.

In the plane, a more complex trajectory with inflection points can be constructed by alternately pushing the needle into tissue for a finite distance and then axially rotating it 180°. For the planar unicycle model, each axial rotation has the effect of changing the sign of the angular velocity constraint (changing the sign on κ). For the planar bicycle model, each axial rotation corresponds to instantaneously turning the front wheel from $+\phi$ to $-\phi$ or vice versa.

While both models generate circular arcs when moving forward, the arcs traced out by the unicycle must be tangent to one another, whereas the arcs traced out by the bicycle need not be. Figure 4 simulates this effect on the trajectory predicted by each model given parameters of κ = 0.05 and ℓ_2 = 2. In this simulation, the input profile was: (1) insert for 1 second at 10 cm/s, (2) rotate 180°, (3) insert for 2 seconds at 10 cm/s, (4) rotate 180°, and (5) insert for 1 second at 10 cm/s.

It is interesting to note that the bevel steering approach does not preclude linear paths for the needle. The needle may be inserted along an approximately straight path by continually rotating it at the base as it is inserted (effectively using a "drilling" motion). When this is done, our models predict a helical needle trajectory with extremely small radius that approximates a line. This effect is observed clinically, and spinning the needle is a recommended surgical technique to reduce the bending that results from the bevel tip (see Wallner, Blasko, and Dattoli 2001, page 8.16).

Generalizing the planar unicycle and bicycle models to full rigid transformations (SE(3)) is the subject of the next section.

2.2. Notation and Definitions

Ultimately, we seek to use the two control inputs, insertion and rotation, to drive a needle to a desired position and orientation in six degrees of freedom (DOF). Since generalized coordinates (such as $(x, y, z,$ roll, pitch, yaw$)$), have singularities, we resort to a coordinate-free representation of the kinemat-

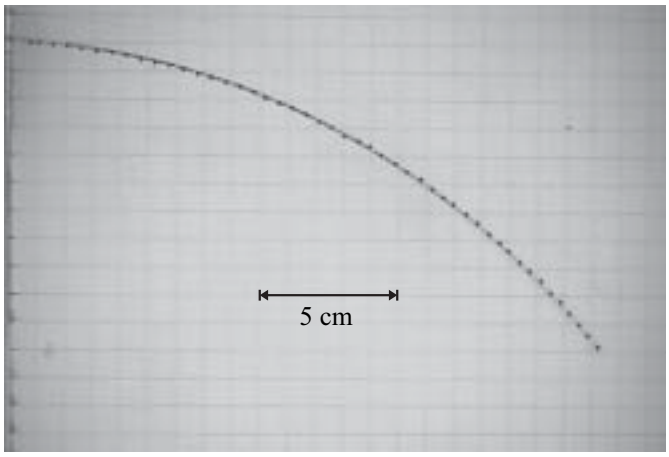

Fig. 2. Tip positions during needle insertion shown overlaid on an image of the final needle path. Tip positions were extracted automatically from a sequence of insertion images.

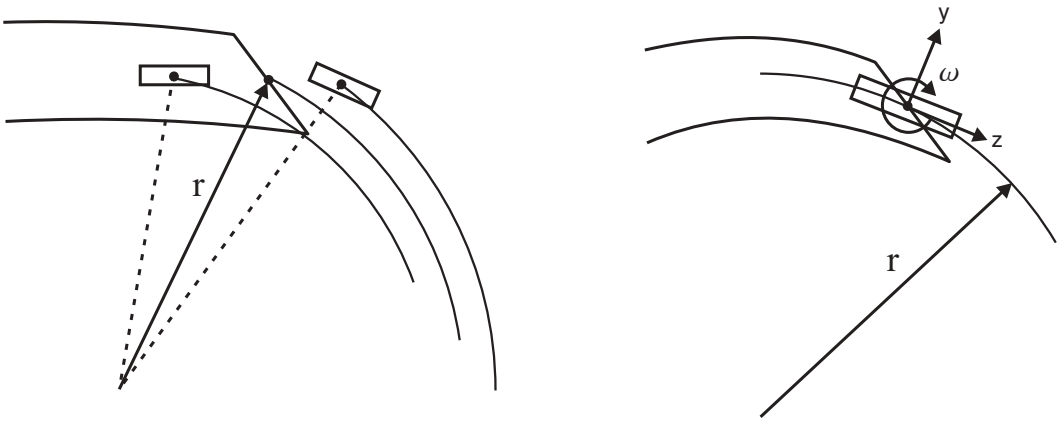

Fig. 3. (Left) The modified planar bicycle model rotates as a rigid body about a center of rotation defined by the intersection of the two wheel axes. (Right) The modified planar unicycle model rolls with an angular velocity proportional to its linear velocity.

ics. Fortunately the kinematic needle equations are quite simple in the coordinate-free representation, but the convenience and generality comes at the added expense of the formalism and notation presented in this section. This section is included for the purpose of establishing notation. We follow the conventions in Murray, Li, and Sastry (1994).

Consider the three reference frames depicted in Figure 1: a stationary world frame, A, and two "body" frames, B and C, attached to the needle tip. Using the homogeneous matrix representation, let

$$g_{ab} = \begin{bmatrix} R_{ab} & p_{ab} \\ 0^T & 1 \end{bmatrix} \in \mathrm{SE}(3) \quad \text{where}$$
$$R_{ab} \in \mathrm{SO}(3), \;\; p_{ab} \in \mathbb{R}^3 \tag{1}$$

denote the rigid transformation between A and B. Likewise, let $g_{bc} = (R_{bc}, p_{bc}) \in \mathrm{SE}(3)$ denote the transformation between B and C.

The isomorphism $\mathbb{R}^3 \simeq \mathrm{so}(3)$ is defined by

$$\widehat{\ }: \begin{bmatrix} \omega_1 \\ \omega_2 \\ \omega_3 \end{bmatrix} \mapsto \begin{bmatrix} 0 & -\omega_3 & \omega_2 \\ \omega_3 & 0 & -\omega_1 \\ -\omega_2 & \omega_1 & 0 \end{bmatrix} \in \mathrm{so}(3),$$
$$^\vee: \begin{bmatrix} 0 & -\omega_3 & \omega_2 \\ \omega_3 & 0 & -\omega_1 \\ -\omega_2 & \omega_1 & 0 \end{bmatrix} \mapsto \begin{bmatrix} \omega_1 \\ \omega_2 \\ \omega_3 \end{bmatrix}, \tag{2}$$

where so(3) is the Lie algebra of SO(3). It will be convenient to "overload" the definitions of $\widehat{\ }$ and $^\vee$ for se(3), the Lie

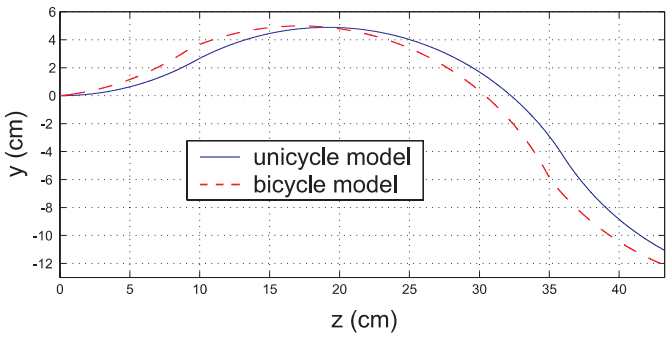

Fig. 4. Comparison of the different planar paths for the one parameter unicycle model and the two parameter bicycle model. Parameters were $\kappa = 0.05$ and $\ell_2 = 2$.

algebra of SE(3). In other words, if $(v, \omega) \in \mathbb{R}^6$, then

$$\widehat{\ }: \begin{bmatrix} v \\ \omega \end{bmatrix} \mapsto \begin{bmatrix} \hat{\omega} & v \\ 0^T & 0 \end{bmatrix} \in \mathrm{se}(3), \quad {}^{\vee}: \begin{bmatrix} \hat{\omega} & v \\ 0^T & 0 \end{bmatrix} \mapsto \begin{bmatrix} v \\ \omega \end{bmatrix}. \quad (3)$$

Given two frames, X and Y, related by the rigid transformation $g_{xy} \in \mathrm{SE}(3)$, the body-frame velocity between them is given by

$$V^b_{xy} = \begin{bmatrix} v^b_{xy} \\ \omega^b_{xy} \end{bmatrix} = (g^{-1}_{xy} \dot{g}_{xy})^{\vee}, \quad \text{where} \quad \begin{aligned} v^b_{xy} &= R^T_{xy} \dot{p}_{xy}, \\ \omega^b_{xy} &= (R^T_{xy} \dot{R}_{xy})^{\vee}. \end{aligned} \quad (4)$$

Given three frames A, B and C moving relative to each other, their body velocities are related by $V^b_{ac} = \mathrm{Ad}_{g^{-1}_{bc}} V^b_{ab} + V^b_{bc}$, where

$$\mathrm{Ad}_g = \begin{bmatrix} R & \hat{p}R \\ 0 & R \end{bmatrix} \quad (5)$$

is the Adjoint operator for a rigid transformation $g = (R, p) \in \mathrm{SE}(3)$.

The unit vectors $e_1, e_2, e_3 \in \mathbb{R}^3$ are the standard basis.

2.3. Nonholonomic Constraints and Control Inputs

In the bicycle model, frames B and C are rigidly connected with parallel x-axes, such that the origin of C is a distance ℓ_1 along the z-axis of B. The y-z plane of C is rotated by angle ϕ about the x-axis, as shown in Figure 1. Thus $R_{bc} = e^{\widehat{e_1}\phi}$ and $p_{bc} = \ell_1 e_3$, where ϕ and ℓ_1 are constants to be determined experimentally as described in Section 3.

There are four Pfaffian constraints, because the velocity of the origin of frame B cannot have a projection along the x or y axis of frame B, and the velocity of the origin of frame C cannot have a projection along the x or y axis of frame C. In other words:

$$e_1^T v^b_{ab} = e_2^T v^b_{ab} = e_1^T v^b_{ac} = e_2^T v^b_{ac} = 0. \quad (6)$$

Since frames B and C are fixed with respect to each other, $V^b_{bc} = 0$. Thus $V^b_{ac} = \mathrm{Ad}_{g^{-1}_{bc}} V^b_{ab} + V^b_{bc} = \mathrm{Ad}_{g^{-1}_{bc}} V^b_{ab}$, and the Pfaffian constraints can be simplified to

$$\begin{bmatrix} 1 & 0 & 0 & 0 & 0 & 0 \\ 0 & 1 & 0 & 0 & 0 & 0 \\ 0 & 0 & 1 & -\frac{1}{\kappa} & 0 & 0 \\ 0 & 0 & 0 & 0 & 1 & 0 \end{bmatrix} V^b_{ab} = 0, \quad (7)$$

where $\kappa = \frac{\tan\phi}{\ell_1}$. Assuming $\ell_1 \neq 0$ and $\phi \in (0, \pi/2)$, a basis V_1, V_2 for the right nullspace of A defines the two allowable directions:

$$V_1 = \begin{bmatrix} v_1 \\ \omega_1 \end{bmatrix} = \begin{bmatrix} e_3 \\ \kappa e_1 \end{bmatrix} \quad \text{and} \quad V_2 = \begin{bmatrix} v_2 \\ \omega_2 \end{bmatrix} = \begin{bmatrix} 0_{3\times 1} \\ e_3 \end{bmatrix}, \quad (8)$$

The vector V_1 corresponds to pure needle insertion, while V_2 corresponds to pure needle shaft rotation.

Since we assume the needle shaft is held in place by the surrounding tissue, the effect of the shaft is to replicate needle base control inputs at the tip. Let $u = (u_1, u_2)$ denote the control inputs, where u_1 is the insertion speed, and u_2 is the shaft rotation speed. This leads to the following kinematic model:

$$V^b_{ab} = u_1 V_1 + u_2 V_2, \quad \text{or, equivalently}$$
$$\dot{g}_{ab}(t) = g_{ab}(t)(u_1 \widehat{V}_1 + u_2 \widehat{V}_2), \quad (9)$$

and

$$n(t) = R_{ab}(t) \ell_2 e_3 + p_{ab}(t). \quad (10)$$

The unicycle model can be viewed as a simpler form of the bicycle model by setting $\ell_2 = 0$ and removing the front wheel of the bicycle. The unicycle model also has four Pfaffian constraints:

$$e_1^T v^b_{ab} = e_2^T v^b_{ab} = e_2^T \omega^b_{ab} = 0, \ \frac{1}{\kappa} e_1^T \omega^b_{ab} = e_3^T v^b_{ab}, \quad (11)$$

the first three of which are straightforward. The fourth constraint above relates the angular velocity of the unicycle about e_1 to the insertion speed, corresponding in the planar case to a circular path with curvature κ. These constraints lead to a constraint matrix identical to that of the bicycle model (7), thus yielding the same allowable directions as before (8). In the unicycle model, n coincides with the origin of frame B, reducing the number of model parameters from two to one by removing ℓ_2.

Summarizing, the two models can be written as follows:

$$\begin{aligned} \dot{g}_{ab}^{-1}(t)g_{ab}(t) &= u_1\widehat{V}_1 + u_2\widehat{V}_2, \\ V_1 &= \begin{bmatrix} e_3 \\ \kappa e_1 \end{bmatrix},\ V_2 = \begin{bmatrix} 0 \\ e_3 \end{bmatrix} \\ n(t) &= R_{ab}(t)\ell_2 e_3 + p_{ab}(t) \quad \text{bicycle model} \\ n(t) &= p_{ab}(t) \qquad\qquad \text{unicycle model } (\ell_2 = 0) \end{aligned} \tag{12}$$

Note that for both the bicycle and unicycle models, the constraints (7) are independent of g_{ab}, and thus the control vector fields are left-invariant. The systems (12) are nonholonomic, since the distribution $\Delta = \text{span}\{V_1, V_2\}$ is not involutive. This can be seen by taking the first Lie bracket of V_1 and V_2 in (12)

$$V_3 = [V_1, V_2] = (\widehat{V}_1\widehat{V}_2 - \widehat{V}_2\widehat{V}_1)^\vee = \begin{bmatrix} 0_{3\times 1} \\ -\kappa e_2 \end{bmatrix}, \tag{13}$$

which is linearly independent of V_1 and V_2 (and thus Δ is not involutive). Successive Lie brackets reveal that the system is of nonholomy degree 4, with a relative growth vector of (2, 1, 2, 1) (Murray, Li, and Sastry 1994, Chapter 7). Therefore, this system is controllable, and we have begun exploring the path planning problem in other work (Park et al. 2005).

2.4. Discrete Model

A discrete implementation of the kinematic model (12) enables simulation and visualization. Advancing the homogeneous transformation, g_{ab}, along V_{ab}^b for T seconds for each time step, $k = 0, 1, 2, \ldots$, yields the discrete-time model

$$\begin{aligned} g_{ab}(k+1) &= g_{ab}(k)e^{(u_1(k)\widehat{V}_1 + u_2(k)\widehat{V}_2)T} \\ n(k) &= R_{ab}(k)\ell_2 e_3 + p_{ab}(k). \end{aligned} \tag{14}$$

The control inputs $u_1(k)$ and $u_2(k)$ now denote the insertion distance and change in rotation angle, respectively, at step k.

3. Experimental Validation

3.1. Materials

A needle driving robot (Figure 5, multimedia extension 1) was designed to control both insertion (u_1) and rotation (u_2) speeds. The insertion subassembly drives the needle by grasping it on the barrel using two opposing rubber wheels actuated by a motor-driven worm gear. Rotation of the needle about its axis is achieved by rotating the insertion subassembly as a unit. Since the wheels grasp the needle tightly by the barrel, rotating the subassembly causes the needle to rotate as well. A slotted needle guide (shown only in the photograph) further fixes the orientation of base of the needle, and thus the bevel direction, relative to the drive wheels. This prevents unwanted needle rotation as the drive wheels turn. Buckling is prevented by passing the needle through a 1.5 mm hole drilled through the aluminum rod that supports the insertion subassembly. This rod extends to the surface of the phantom tissue into which the needle is inserted.

The needle used in the experiments was a 0.7 mm diameter solid nitinol cylinder (simulating a 22 gauge needle) with a smooth surface finish and a hand-machined bevel tip of 45° (multimedia extension 2). The phantom tissue material used in this experiment was Simulated Muscle Ballistic Test Media (SimTest) from Corbin, Inc. This material qualitatively feels similar to human muscle, and is stiff enough (4.9 N/mm by a blunt indentation test) relative to our superelastic needle to satisfy our modeling assumption that macroscopic displacement of the tissue by the needle will not occur. As mentioned in Section 2, this means that the needle shaft will follow the tip as it cuts through the tissue. This is the same set of needle and phantom materials used in Webster, Memisevic, and Okamura (2005), where this was shown to be a good modeling assumption for this needle/tissue combination.

It is expected that similar results can be obtained in phantom tissues with a wide range of properties by selecting the appropriate needle stiffness. While the SimTest media, which is qualitatively similar to muscle, is stiffer than some organs (e.g., liver), we expect our modeling assumption to hold even in softer tissues if we increase the flexibility of the needle shaft. Quantifying the properties of living tissue is an active research area. As these properties are quantified more fully, our understanding of the effect of needle shaft properties on steering will improve. Our nitinol needle and SimTest media represent a specific example of a needle/tissue pair with appropriately matched properties. This results in a significant steering capability and fits our modeling assumption. Initial experiments indicate that bevel tip needles can steer well even in needle/tissue combinations that are not as well matched (e.g., softer tissue, stiffer needle), but the shapes they take on may change to some degree. This is a topic of future research, discussed in more detail in Section 4.

The rubber-like SimTest media was cast into a sheet approximately 15 mm thick, and the needle was introduced vertically, as shown in multimedia extension 3. To collect coordinates describing the needle path in each insertion, a physical grid was overlaid on the phantom tissue. A 1 cm square grid was laser etched into a clear polycarbonate sheet so that digital images could be taken of the needle path through the grid (Figure 5). Thirty two points along the needle path were recorded in pixel coordinates for each run. These pixel coordinates were

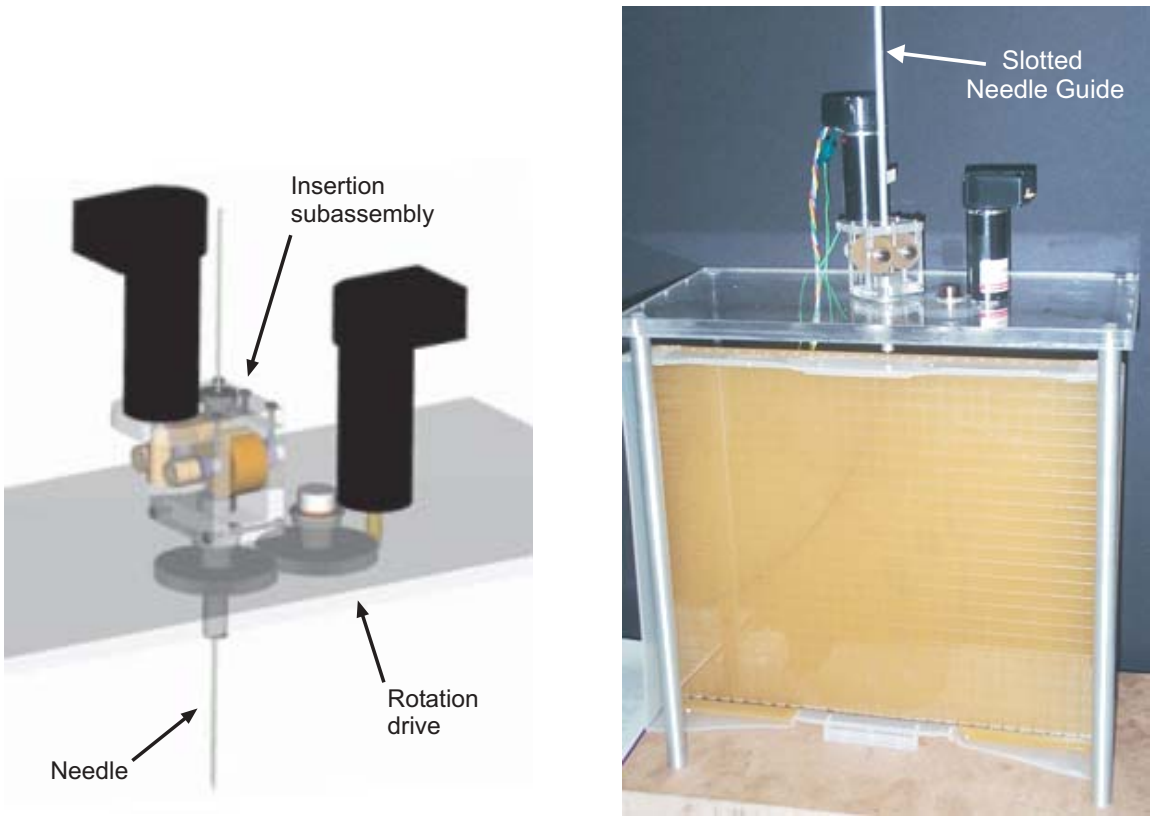

Fig. 5. A needle driving robot for steering of flexible needles: CAD model (left) and experimental assembly (right).

converted to physical coordinates in a frame attached to the polycarbonate grid using the following procedure.

Nine calibration points (grid intersections), distributed evenly across the planar grid, were obtained in both pixel coordinates and physical coordinates. Then, using a 2-dimensional version the Direct Linear Transform (DLT) algorithm, the projective transformation was estimated from the point correspondences for each run. These transformations enabled us to express coordinates along the needle in the physical coordinate system. We estimate the error associated with this collection process to be within ± 1 mm. The nonholonomic model was fit to this physical data as described in the following section.

3.2. Experimental Procedure

The needle described previously was inserted multiple times into a single phantom tissue sample for all experiments. Care was taken to insert the needle at a different location each time so that the holes cut by previous experiments would not affect subsequent trials. Because the phantom tissue is semi-opaque, visualizing the needle with an optical camera requires it to stay within a few millimeters of the surface. Doing so requires control of axial needle rotation (bevel direction), or the needle may dive below the surface or rise above it (out of the phantom tissue). This diving or rising effect is a result of small errors in initial needle rotation calibration that can cause the needle bending plane to be slightly misaligned with phantom tissue surface. Accurate control of needle axial rotation requires the needle steering model parameters that these experiments are designed to reveal. However, the needle can be kept in a plane just below the surface of the tissue by manually making slight corrections to the axial rotation of the needle as necessary to minimize out of plane motion. In contrast to the rotational degree of freedom, the linear insertion velocity is constant, and is computer controlled. Possible sources of error in these experiments include initial insertion angle from vertical, human controlled (approximately constant) spin angle, slippage of drive wheels relative to the shaft (not visually perceptible), small deformations of the phantom tissue, and identification of points on the needle path in digital images.

Two sets of input parameters were used in the experimental insertions. In one, u_2 was set to zero, and the needle was inserted at a constant u_1 to a depth of 235 mm. This created a "single bend" insertion profile. In the other, u_2 was set to zero for the first 1/3 of the total insertion depth (83.3 mm). Then

u_1 was set to zero and the needle was rotated 180 degrees. Finally, with u_2 again fixed at zero, the needle was inserted the remaining 2/3 of the insertion depth at constant u_1, until the needle reached a total insertion depth of 250 mm. This created an S-shaped or "double bend" insertion profile. A total of 13 insertions were performed, composed of eight single bend insertions and five double bend insertions.

When the insertion speed u_1 is constant and needle rotation does not change ($u_2 = 0$), the needle tip follows a planar circular arc as described in Section 2. This arc is a function of the parameters κ and ℓ_2. To fit all 13 trials simultaneously, the parameter set was expanded to include two unique "nuisance parameters" for each individual trial. These parameters were y_o^j (the y entry point of the needle) and γ^j (the initial angle of needle with respect to the z axis in the y-z plane) for each run, $j = 1, \ldots, 13$. The γ^j parameter was included because it was observed that while all insertions had similar basic shape and curvature properties, they differed by a slight rotation indicative of a small amount of error in initial entry angle. This error was probably caused by the needle tip deforming the surface of the rubber before puncturing it, and deflecting the angle of entry a small amount in the process. The vector of parameters is given by $\theta = (\kappa, \ell_2, y_o^1, \gamma^1, \ldots, y_o^{13}, \gamma^{13})$.

While it is possible to integrate the path of the needle using the Lie group expressions given in Section 2 (which is done to generate the plots in Section 3.3), the nonlinear parameter estimation is greatly facilitated with a closed form expression for the needle trajectory. This allows the nonlinear fitting algorithm to run much more efficiently, and eliminates small errors associated with the integration time step. It is straightforward in the planar case to derive such an expression for the needle path in terms of the circular segments that describe it.

For a single run of the bicycle model (j superscript omitted for clarity), the radius of the arcs (all have the same radius) is

$$r = \frac{1}{\kappa} = \sqrt{{\ell_2}^2 + (\ell_1 \cot(\phi))^2}. \tag{15}$$

The position of the center of the first arc is

$$c_1 = \begin{bmatrix} 0 \\ y_o \pm r\cos(\sin^{-1}(\ell_2\kappa) + \gamma) \\ \pm r\sin(\sin^{-1}(\ell_2\kappa) + \gamma) \end{bmatrix}, \tag{16}$$

where the $\pm$ is selected by whether the arc points toward the positive or negative y direction. The center of subsequent circular arcs (after rotating u_2 by 180°) is given by a similar expression where the nuisance parameters have been replaced by the ending conditions of the previous arc (denoted by the leading superscript e):

$$c_i = \begin{bmatrix} 0 \\ {}^e y_{i-1} \pm r\cos(\sin^{-1}(\ell_2\kappa) + {}^e\gamma_{i-1}) \\ {}^e z_{i-1} \pm r\sin(\sin^{-1}(\ell_2\kappa) + {}^e\gamma_{i-1}) \end{bmatrix}. \tag{17}$$

For a single run of the unicycle model, the radius of the arcs is

$$r = \frac{1}{\kappa}. \tag{18}$$

The position of the center of the first arc simplifies to

$$c_1 = \begin{bmatrix} 0 \\ y_o \pm r\cos(\gamma) \\ \pm r\sin(\gamma) \end{bmatrix}, \tag{19}$$

and the center of subsequent circular arcs similarly simplifies to

$$c_i = \begin{bmatrix} 0 \\ {}^e y_{i-1} \pm r\cos({}^e\gamma_{i-1}) \\ {}^e z_{i-1} \pm r\sin({}^e\gamma_{i-1}) \end{bmatrix}. \tag{20}$$

Given these circle centers, the desired $\hat{z}$ prediction for a value y is then given by the equation for a circle:

$$\begin{aligned} &f(z,\theta) = e_2^T c_i + \sqrt{r^2 - (z - e_3^T c_i)^2} \\ &e_3^T\, {}^e c_{i-1} \le z \le e_3^T\, {}^e c_i, \end{aligned} \tag{21}$$

where e_2 and e_3 are standard basis vectors such that, for example, $e_2^T c_i$ denotes the y component of the center of the i^{th} circle segment.

This closed-form model can now be fit to the experimental data using Matlab's `nlinfit` command. This function numerically computes a Jacobian in terms of the parameters,

$$J = \frac{\partial f}{\partial \theta}. \tag{22}$$

It then uses the Gauss-Newton gradient descent method to minimize the residual error between the observed data points and the predicted ones.

3.3. Results

For the bicycle model, the experimentally fit parameters were $\kappa = 0.0449$ and $\ell_2 = 2.3775$ cm, with 95% confidence intervals of $\pm$ 0.0006 and $\pm$ 0.1498 respectively. Note that κ can be directly related back to bicycle steering angle (ϕ) and distance between the wheels (ℓ_1), since κ is a function of both. For example, choosing ℓ_1 = 4 cm yields a steering angle of ϕ = 10.18°. Figures 6 and 7 show plots of the single bend and double bend fitted models along with mean data values and standard deviation bars for each data point, with the nuisance parameters taken into account. The plots were generated by integrating the Lie group expressions given in Section 2.

The experimentally fit parameter for the unicycle model was $\kappa = 0.0468$ with a 95% confidence interval of $\pm$ 0.0001. Since the unicycle model can be viewed as a simpler form of the bicycle model, we can use a hypothesis test to determine whether the second parameter in the bicycle model represents a statistical improvement in describing the needle trajectory

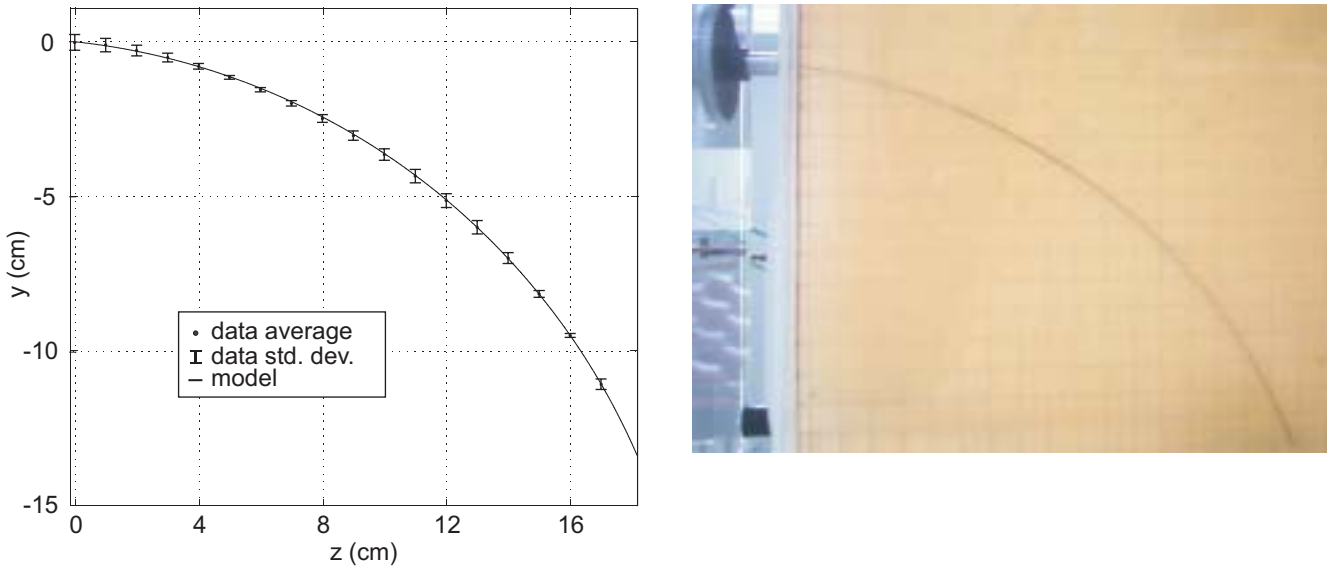

Fig. 6. (Left) The bicycle nonholonomic model prediction for a single curve run, shown with average data (including nuisance parameters) and standard deviation bars. (Right) During the experiment, the needle was inserted 23.5 cm, without spin.

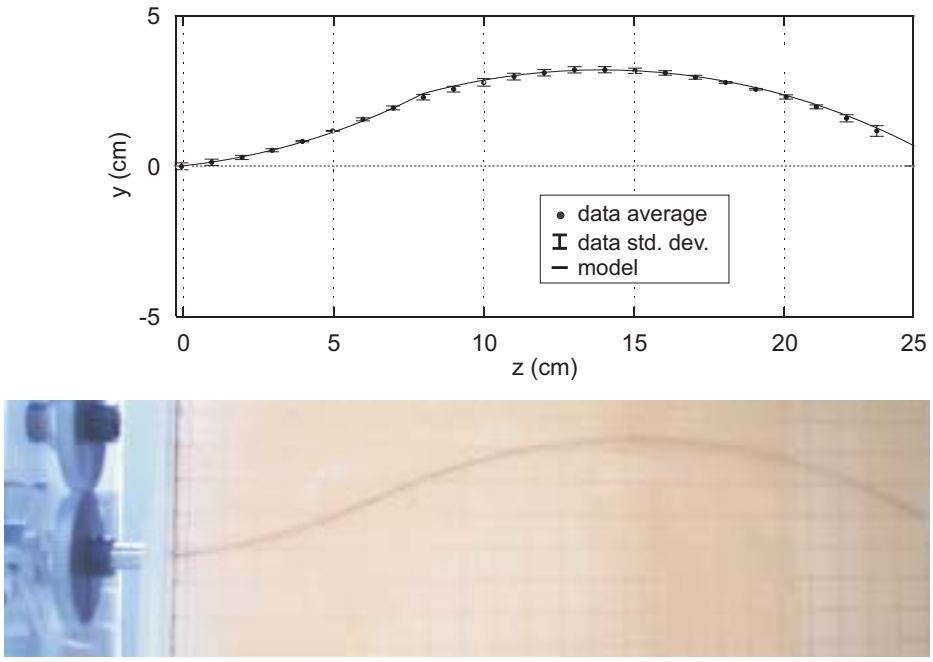

Fig. 7. (Top) The bicycle nonholonomic model prediction for a run with two curves, shown with average data (including nuisance parameters) and standard deviation bars. (Bottom) During the experiment, the needle was inserted 8.3 cm, spun 180°, then inserted another 16.7 cm.

over the unicycle model (null hypothesis). A t-test with $\alpha = 0.01$ leads to rejection of the null hypothesis, ($P < 0.01$) and we conclude that the bicycle model is statistically significantly better at describing the data. This is illustrated graphically in Figures 8 and 9.

As shown in Figures 6 and 7, the bicycle model qualitatively fits the data very well. Quantitatively, the root mean squared error between the model prediction and the observed data points is 1.3 mm for the bicycle model, compared to 2.6 mm for the unicycle model. The error for the bicycle model is quite low, however it is slightly above our measurement error estimate of ± 1 mm, so there may be a small amount of inherent variability in the data not captured by our kinematic model.

4. Discussion

We have presented a pair of kinematic models that describe the trajectory of a flexible needle with a bevel tip. Experiments and statistical analysis verify that the two-parameter "bicycle" model describes the needle behavior better than a single-parameter "unicycle" model. The path predicted by the two-parameter model is in close agreement with our experimental data, but there remain several points to consider for future improvements of the model, and future enhancements to experimental procedures. One is the modeling assumption that the needle and tissue be matched so that the tissue is stiff relative to the needle.

If the needle and tissue are not perfectly matched (e.g., the same needle is used with softer tissue), simulations indicate that the shape of the needle path will change (Alterovitz, Goldberg, and Okamura 2005a). However, our model in stiff tissues may still provide a basis for control. It can be incorporated into finite element models (FEM) of tissue to predict the needle path in softer tissues. An example is Alterovitz, Goldberg, and Okamura (2005a), where our model provides an idea of where the needle tip will deflect as it severs nodes of the FEM tissue mesh. The basic model can also be used for planning in conjunction with dynamic programming for unmatched needle/tissue combinations (Alterovitz et al. 2005b). While the model and experiments in the matched setting described in Section 3 provide a first step toward analytical representations of needle shape in an unmatched setting, future research is needed in this area. Even in the absence of such analytical representations, our model may be useful for higher rate control than is currently possible with FEM techniques, since they are computationally intensive.

There are also some other interesting issues arising from physical considerations that it may be possible to build into our model. One physical consideration is that the trajectory of an actual needle intuitively ought to be at least once-differentiable. Both the bicycle and unicycle models will be once-differentiable as long as the needle insertion does not stop ($u_1 = 0$) when the bevel is re-oriented ($u_2 \neq 0$). But for the bicycle model, if rotation happens without simultaneous linear insertion, a small "kink" (the non-tangent circles mentioned in Section 2.1) will result. Another physical consideration is that needles have finite torsional stiffness. As the shaft of the needle is made more flexible to enhance bending, it will also become more torsionally flexible. We have considered possible modifications to our basic kinematic model that may help remove the kink phenomenon and take torsional stiffness into account. The models described in Section 2, both have the following body velocity structural form, amenable to numerical integration (9):

$$V_{ab}^{b} = \begin{bmatrix} 0 & 0 & u_1 & \kappa u_1 & 0 & u_2 \end{bmatrix}^T, \tag{23}$$

where u_1 is the insertion velocity and u_2 is the shaft rotation velocity. One possible way to modify this model is through alternative descriptions of the parameters, and another is to add new parameters.

To account for torsional stiffness, it may be useful to add a new parameter, for example $\omega_{\text{tip}} = \alpha u_2$, where α may be a nonlinear function of time or arclength that appropriately captures the effects of friction and torsional stiffness. The human controlling the rotational degree of freedom in our experiments (as described in Section 3) compensated for torsional stiffness effects by rotating the needle base further than the desired tip rotation. Both torque information sensed at the fingers and visual observations of the needle tip may have been useful to the human to keep the needle in plane. To enable automation of this, one area of device improvement we will pursue is incorporating a torque sensor into the robotic needle driving mechanism. This will make torque measurements available to the controllers we develop. As one would expect, the base of the needle must be turned further for a given desired tip motion the further the needle is inserted into rubber, because overall frictional force between the needle shaft and the tissue increases with insertion depth. We hypothesize that a controller to replace the human in controlling the rotational degree of freedom may have to take this into account through modeling and/or sensing.

It must be emphasized that it is not clear that this compensation for torsional stiffness will be necessary in live tissues. They contain inherent lubrication (blood), and we expect them to have far less friction with the needle shaft than is observed in rubber phantoms. It may also be possible to reduce friction by using various gels (containing water or other liquid) as the phantom tissue, presumably more closely replicating the interaction between the needle and human tissue.

Steering directly in *in vivo* or *ex vivo* tissues introduces many new phenomena that must be modeled, including membrane pop-through effects, as well as tissue inhomogeneity and anisotropy. While these may be challenging to model, they do not appear to preclude steering needles using bevel tip forces. Figure 10 shows a fluoroscope image of a needle inserted into bovine muscle. It is clear that bending still oc-

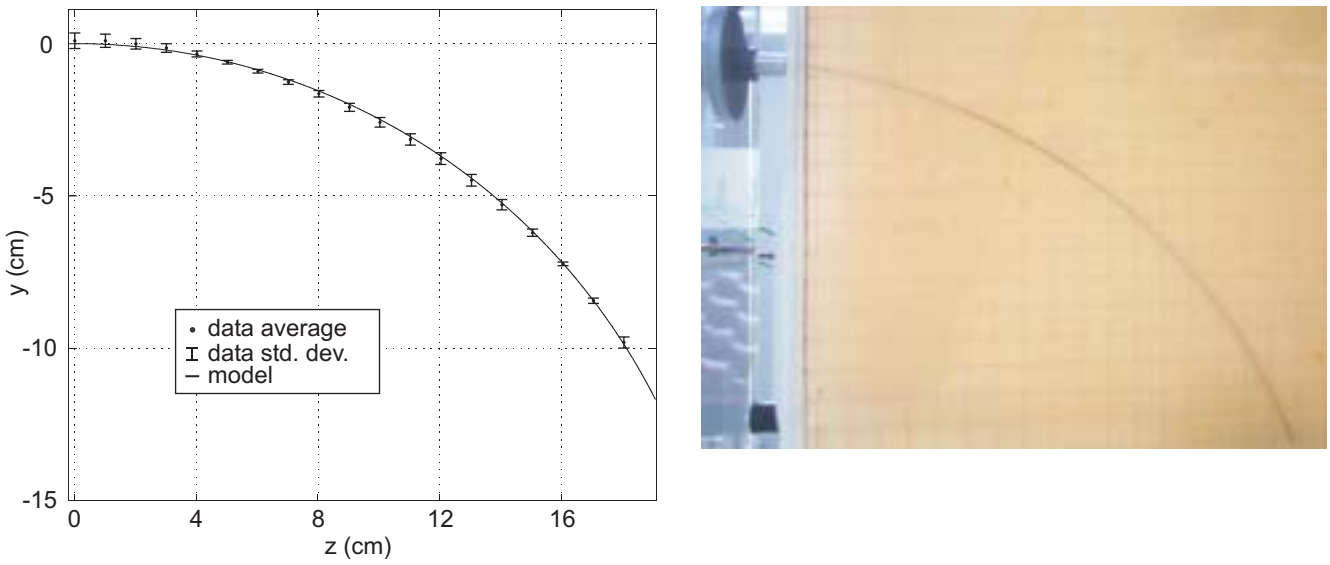

Fig. 8. (Left) The unicycle nonholonomic model prediction for a single curve run, shown with average needle path data (including nuisance parameters) and standard deviation bars. (Right) Photograph of one needle insertion.

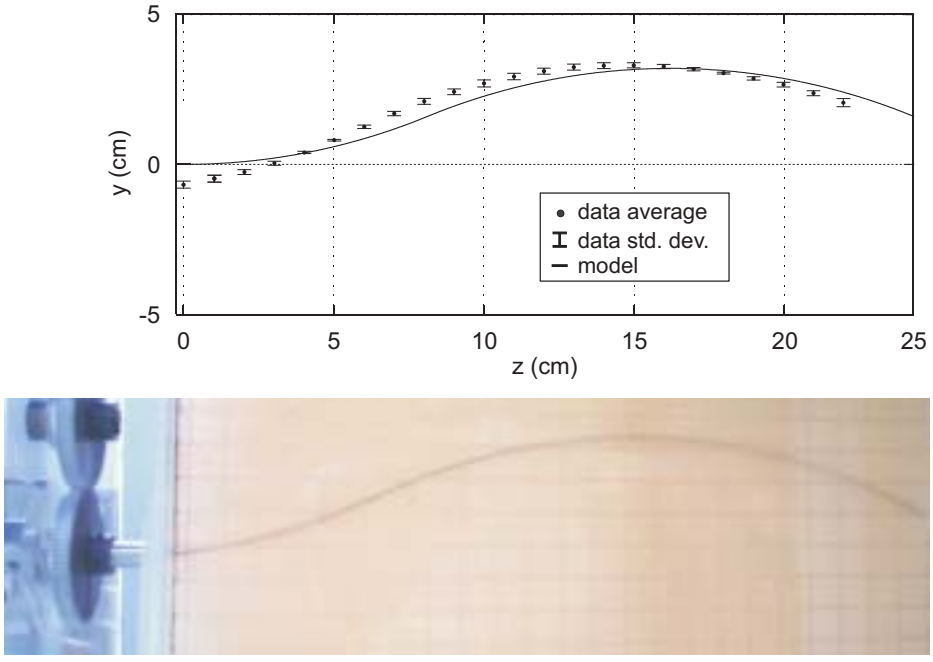

Fig. 9. (Top) The unicycle nonholonomic model model prediction for a run with two curves, shown with average needle path data (including nuisance parameters) and standard deviation bars. The single parameter model is not able to fully capture the curvature variations of the physical needle. (Bottom) Photograph of one needle insertion.

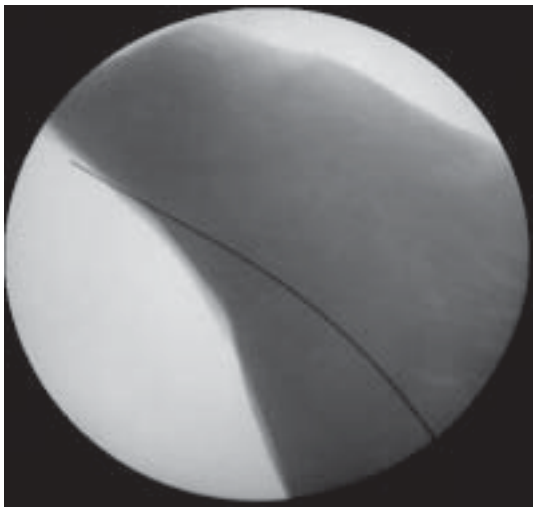

Fig. 10. This fluoroscope image demonstrates that a 0.6 mm diameter bevel tip nitinol needle can steer through bovine muscle. While moving from homogeneous rubber phantoms to real tissue introduces new modeling challenges, this image shows that bevel based steering is not limited to homogeneous rubber phantoms.

curs in this more realistic environment. It not known precisely what other effects will be seen in live tissues, but it is possible that some of these effects may enhance bevel tip steering by allowing tighter curvatures to be realized, while others may reduce curvature.

To account for the kink we believe that it may not be necessary to add an additional parameter to the model, but rather to change the description of an existing parameter. Rather than considering κ a constant, we can considering it a function of time and/or arclength. It may also be possible to use this new κ function to account for some of the effects of tissue deformation, either as an alternative to or in collaboration with FEM methods. There may also exist useful alternative descriptions of needle trajectory in terms of differential equations. The general form might be

$$M\ddot{V}_{ab}^{b} + C\dot{V}_{ab}^{b} + KV_{ab}^{b} = U, \tag{24}$$

where M, C, K are constant matrices including general parameters, and U is an input body velocity, which can be a function of time or arclength, or both.

Investigating these modified and alternative descriptions of needle kinematics is an area for future work, that will be pursued if they begin to show significant advantages over current techniques. When investigating new models, it will be critical to ensure that the model does not over-fit the data for a particular set of experiments. The model should be general and applicable to various needles and tissues, but without undue complexity or redundancy. To ensure this, a statistical analysis of model parameters such as the one carried out in this paper is critical.

In addition, the use of a control system with image feedback will mitigate the need for a perfect, patient-specific model. However, imaging measurements will include noise, and some forms also expose the patient (and the physician) to radiation, possibly reducing the maximum sensor update rate. As we draw nearer to clinical application of needle steering, we will seek a practical balance between a priori path planning based entirely on models and control through image feedback.

Enhancements to experimental sensing are also possible to improve data accuracy and to make 3D measurements. Stereo cameras and transparent phantom tissues will facilitate this. If tissues are not transparent, we may substitute radiological imagers such as fluoroscopes for the optical cameras. In either case, it will be useful to have the needle embedded deeper in the tissue to enable more complex 3D trajectories. For optical cameras, this will require calibration algorithms to compensate for optical refraction at the surface of the tissue. (We neglected refraction in this paper because the needle was so near the tissue surface.) In future work, we also plan to track the needle as it progresses through the tissue rather than collecting points along the needle shaft after it has reached its final position, as was done in this paper. While post-insertion collection is accurate for the matched needle/tissue combination in our experiments (Figure 2), it may not be for combinations that are not as well matched. It will also be useful to track tissue deformation in three dimensions, perhaps using fiducial markers embedded in the phantom. We note that, to the best of our knowledge, no previous needle insertion modeling work (see Section 1) has recorded 3D needle insertions in real or phantom tissues that include bending, steering, or tissue deformation.

5. Conclusion and Future Work

Steering flexible needles using a bevel tip has the potential to enable accurate, dexterous targeting for percutaneous medical procedures in a manner that minimizes tissue deformation and damage. The first step in steering a needle to a desired location is a kinematic analysis of the needle path. This paper introduced a 6-DOF nonholonomic model based on steering due to bevel tip asymmetry. Using a robotic mechanism designed for flexible needle insertion, we demonstrated that our model accurately predicts the path of a compliant needle through phantom tissue when the needle and tissue are appropriately matched (the tissue is stiff relative to the needle). A nitinol needle and rubber phantom qualitatively similar to human muscle provide an example of a matched pair. In particular, we demonstrated by statistical analysis that a two-parameter bicycle model can describe the needle steering behavior better than a one-parameter unicycle model. As discussed in Sec-

tion 4, more detailed kinematic models, together with improved experimental methods, are expected to enable accurate 3D needle control for a wider variety of tissue and needle parameters.

This work facilitates a broader study to improve the accuracy of needle targeting for clinical and research applications. Ongoing and future research activities include:

- Determining the relationship of the bevel angle to the steering angle ϕ (Webster, Memisevic, and Okamura 2005).
- Creating a noise model that captures the inherent variability of needle insertion and tissue inhomogeneity, and incorporates these stochastic features into planning (Park et al. 2005).
- Integrating needle steering models into simulations that include large tissue deformation (Alterovitz et al. 2005).
- Path planning for steering needles around obstacles (e.g. bones, delicate structures, etc.) in order to acquire targets not previously accessible (Alterovitz, Goldberg, and Okamura 2005; Alterovitz et al. 2005).
- Selection of optimal insertion points (Alterovitz et al. 2005).
- Development of a complete system for needle steering that uses feedback from medical imaging to enhance accuracy in the presence of unmodeled tissue deformation and inhomogeneity.

Appendix: Index to Multimedia Extensions

The multimedia extension page is found at http://www.ijrr.org.

Table of Multimedia Extensions

Extension	Type	Description
1	Video	robotic_needle_driver.mp4 Video of a robot designed to insert flexible needles
2	Video	needle_flexibility.mp4 Demonstrates the asymmetric bevel tip and the superelasticity of nitinol needles
3	Video	needle_in_rubber.mp4 Video of experiments in rubber phantoms with model-based simulations

Acknowledgments

This work was supported in part by the National Institutes of Health grant R21-EB003452, National Science Foundation grant IIS 0098382, and a National Defense Science and Engineering Graduate Fellowship. The authors thank Joshua Wainer for assistance in data collection, Ken Goldberg and Ron Alterovitz for their ideas contributing to this work, and Gabor Fichtinger for sharing his clinical application expertise.

References

Alterovitz, R., Goldberg, K., and Okamura, A. 2005a. Planning for steerable bevel-tip needle insertion through 2D soft tissue with obstacles. *IEEE International Conference on Robotics and Automation*, pp. 1652–1657.

Alterovitz, R., Lim, A., Goldberg, K., Chirikjian, G. S., and Okamura, A. 2005b. Planning for steerable bevel-tip needle insertion through 2d soft tissue with obstacles. *IEEE/RSJ International Conference on Intelligent Robots and Systems*, pp. 120–125.

Alterovitz, R., Goldberg, K., Pouliot, J., Taschereau, R., and Hsu, I.-C. 2003a. Needle insertion and radioactive seed implantation in human tissues: Simulation and sensitivity analysis. *IEEE International Conference on Robotics and Automation*, pp. 1793–1799.

Alterovitz, R., Goldberg, K., Pouliot, J., Taschereau, R., and Hsu, I.-C. 2003b. Sensorless planning for medical needle insertion procedures. *IEEE/RSJ International Conference on Intelligent Robots and Systems*, pp. 3337–3343.

Alterovitz, R., Pouliot, J., Taschereau, R., Hsu, I.-C., and Goldberg, K. 2003c. Simulating needle insertion and radioactive seed implantation for prostate brachytherapy. In *Medicine Meets Virtual Reality 11*, (ed. J. D. Westwood) pp. 19–25. IOS Press.

Blasko, J. C., Mate, T., Sylvester, J. E., Grimm, P. D., and Cavanagh, W. 2002. Brachytherapy for carcinoma of the prostate: techniques, patient selection, and clinical outcomes. *Seminars in Radiation Oncology* 12(1):81–94.

Boctor, E., Webster, R. J. III, Mathieu, H., Okamura, A. M., and Fichtinger, G. 2004. Virtual remote center of motion control for needle placement robots. *Journal of Computer-Aided Surgery* 9(5):175–183.

Brett, P. N., Harrison, A. J., and Thomas, T. A. 2000. Schemes for the identification of tissue types and boundaries at the tool point for surgical needles. *IEEE Transactions on Information Technology in Biomedicine* 42(1):30–36.

Brett, P. N., Harrison, A. J., Thomas, T. A., and Carr, A. 1997. Simulation of resistance forces acting on surgical needles. *Proceedings of the Institution of Mechanical Engineers* 211 (H4):335–347.

Cleary, K., Banovac, F., Lindisch, D., and Watson, V. 2001. Robotically assisted spine needle placement: program plan and cadaver study. *14th IEEE International Symposium on Computer Based Medical Systems*, pp. 339–342.

Cooperberg, M. R., Lubeck, D. P., Meng, M. V., Mehta, S. S., and Carroll, P. R. 2004. The changing face of low-risk

prostate cancer: trends in clinical presentation and primary management. *Clin Oncol* 22(11):2141–2149.

Daum, W. 2003. A deflectable needle assembly. U.S. Patent 5,572,593.

DiMaio, S. P. and Salcudean, S. E. 2003a. Needle insertion modeling and simulation. *IEEE Transactions on Robotics and Automation* 19(5):864–875.

DiMaio, S. P. and Salcudean, S. E. 2003b. Needle steering and model-based trajectory planning. *Medical Image Computing and Computer-Assisted Intervention*, pp. 33–40.

Fung, Y. C. 1993. *Biomechanics: Mechanical Properties of Living Tissues, 2nd Edition*. New York: Springer-Verlag.

Gibson, S. F. and Mirtich, B. 1997. A survey of deformable modeling in computer graphics. Technical report, MERL, TR-97-19.

Glozman, D. and Shoham, M. 2004. Flexible needle steering and optimal trajectory planning for percutaneous therapies. In *Medical Image Computing and Computer Assisted Intervention*, (eds C. Barillot, D. Haynor, and P. Hellier), volume 3217 of Lecture Notes in Computer Science, pp. 137–144. Springer.

Gorman, P., Krummel, T., Webster, R., Smith, M., and Hutchens, D. 2000. A prototype haptic lumbar puncture simulator. *Proceedings of Medicine Meets Virtual Reality*, pp. 106–109.

Guo, S., Fukuda, T., Nakamura, T., Arai, F., Oguro, K., and Negoro, M. 1996. Micro active guide wire catheter system—characteristic evaluation, electrical model and operability evaluation of micro active catheter. *IEEE International Conference on Robotics and Automation*, pp. 2226–2231.

Haga, Y., Tanahashi, Y., and Esashi, M. 1998. Small diameter active catheters using shape memory alloy. *Proceedings of IEEE Micro Elector Mechanical Systems*, pp. 419–424.

Hayashi, K., Abe, H., and Sato, M. 1996. *Data Book on Mechanical Properties of Living Cells, Tissues, and Organs*. New York: Springer.

Hiemenz, L., McDonald, J. S., Stredney, D., and Sessanna, D. 1996. A physiologically valid simulator for training residents to perform an epidural block. *Proceedings of the IEEE Biomedical Engineering Conference*, pp. 170–173.

Jemal, A. 2004. Cancer statistics, 2004. *CA Cancer J Clin* 54(8).

Kaiser, W. A., Fischer, H., Vagner, J., and Selig, M. 2000. Robotic system for biopsy and therapy of breast lesions in a high-field whole-body magnetic resonance tomography unit. *Investigative Radiology* 35:513–519.

Kataoka, H., Washio, T., Audette, M., and Mizuhara, K. 2001. A model for relations between needle deflection, force, and thickness on penetration. *Medical Image Computing and Computer-Assisted Intervention*, pp. 966–974.

Kataoka, H., Washio, T., Chinzei, K., Mizuhara, K., Simone, C., and Okamura, A. 2002. Measurement of tip and friction force acting on a needle during penetration. In *Medical Image Computing and Computer Assisted Intervention*, (eds T. Dohi and R. Kikinis), volume 2488 of Lecture Notes in Computer Science, pp. 216–223. Springer.

Koyama, H., Uchida, T., Funakubo, H., Takakura, K., and Fankhauser, H. 1990. Development of a new microsurgical robot for stereotactic neurosurgery. *Stereotactic Functional Neurosurgery* 54-55:462–467.

Krouskop, T. A., Wheeler, T. M., Kallel, F., Garria, B. S., and Hall, T. 1998. Elastic moduli of breast and prostate tissues under compression. *Ultrasonic Imaging* 20.

Lim, G., Park, K., Sugihara, M., Minami, K., and Esashi, M. 1996. Future of active catheters. *Sensors and Actuators* 56:113–121.

Mahvash, M. and Hayward, V. 2002. Haptic rendering of cutting: A fracture mechanics approach. *Haptics-e: The Electronic Journal of Haptics Research* (www.haptics-e.org) 2(3).

Masamune, K., Fichtinger, G., Patriciu, A., Susil, R. C., Taylor, R. H., Kavoussi, L. R., Anderson, J. H., Sakuma, I., Dohi, T., and Stoianovici, D. 2001. System for robotically assisted percutaneous procedures with computed tomography guidance. *Computer Aided Surgery* 6(6):370–383.

Masamune, K., Kobayashi, E., Masutani, Y., Suzuki, M., Dohi, T., Iseki, H., and Takakura, K. 1995. Development of an MRI-compatible needle insertion manipulator for stereotactic neurosurgery. *Journal of Image Guided Surgery* 1:242–248.

Mayer, S. A. 2003. Ultra-early hemostatic therapy for intracerebral hemorrhage. *Stroke* 34(1):224–9.

Mulier, S., Ni, Y., Miao, Y., Rosiere, A., Khoury, A., Marchal, G., and Michel, L. 2003. Size and geometry of hepatic radiofrequency lesions. *Eur J Surg Oncol* 29(10):867–78.

Murray, R. M., Li, Z., and Sastry, S. S. 1994. *A Mathematical Introduction to Robotic Manipulation*. CRC Press, Ann Arbor MI.

Nakakura, E. and Choti, M. 2000. Hepatocellular carcinoma: Current management recommendations. *Advances on Onc* 16(2):12–18.

Nienhuys, H. W. and van der Stappen, A. 2001. A surgery simulation supporting cuts and finite element deformation. In *Medical Image Computing and Computer-Assisted Intervention*, (eds W. J. Niessen and M. A. Viergever), pp. 153–160. Springer-Verlag.

Nienhuys, H. W. and van der Stappen, A. 2004. A computational technique for interactive needle insertions in 3d nonlinear material. *IEEE International Conference on Robotics and Automation*, pp. 2061–2067.

Okamura, A. M., Simone, C., and O'Leary, M. D. 2004. Force modeling for needle insertion into soft tissue. *IEEE Transactions on Biomedical Engineering* 51(10):1707–1716.

Okazawa, S., Ebrahimi, R., Chuang, J., Salcudean, S. E., and Rohling, R. 2005. Hand-held steerable needle device. *IEEE/ASME Transactions on Mechatronics* 10(3):285–296.

O'Leary, M. D., Simone, C., Washio, T., Yoshinaka, K., and

Okamura, A. M. 2003. Robotic needle insertion: Effects of friction and needle geometry. *IEEE International Conference on Robotics and Automation*, pp. 1774–1780.

Park, W., Kim, J. S., Zhou, Y., Cowan, N. J., Okamura, A. M., and Chirikjian, G. S. 2005. Diffusion-based motion planning for a nonholonomic flexible needle model. *IEEE International Conference on Robotics and Automation*, pp. 4611–4616.

Potamianos, P., Davies, B. L., and Hibberd, R. D. 1994. Intraoperative imaging guidance for keyhole surgery: methodology and calibration. *International Symposium on Medical Robotics and Computer Assisted Surgery*, Pittsburgh, PA.

Stoianovici, D. 2001. Urobotics - urology robotics at Johns Hopkins. *Computer Aided Surgery* 6(6):360–369.

Stoianovici, D., Webster, R., and Kavoussi, L. 2005. Surgical robotic applications in minimally invasive urooncology surgery. In *Complications of Urologic Laparoscopic Surgery: Recognition, Management and Prevention*, (eds R. Moore and J. Bishoff), pp. 353–363. Taylor and Francis. ISBN 1-84184-566-3.

Taylor, R. H., Funda, J., Eldridge, B., Gomory, S., Gruben, K., LaRose, D., Talamini, M., Kavoussi, L., and Anderson, J. 1995a. A telerobotic assistant for laparoscopic surgery. *IEEE Engineering in Medicine and Biology Magazine* 14(3):279–288.

Taylor, R. H., Funda, J., Grossman, D. D., Karidis, J. P., and LaRose, D. A. 1995b. Remote center-of-motion robot for surgery. U.S. Patent 5,397,323.

Ulmer, S. C. 2000. Hepatocellular carcinoma: a concise guide to its status and management. *Postgrad Med* 107(5):117–24.

Wallner, K., Blasko, J. C., and Dattoli, M. 2001b. *Prostate Brachytherapy Made Complicated*. SmartMedicine Press, Seattle, Washington, second edition.

Webster, R. J. III, Cowan, N. J., Chirikjian, G. S., and Okamura, A. M. 2006. Nonholonomic Modeling of Needle Steering. 9th International Symposium on Experimental Robotics. *Springer Tracts in Advanced Robotics* 21:35–44.

Webster, R. J. III, Memisevic, J., and Okamura, A. M. 2005. Design considerations for robotic needle steering. *IEEE International Conference on Robotics and Automation*, pp. 3599–3605.

Yanof, J., Haaga, J., Klahr, P., Bauer, C., Nakamoto, D., Chaturvedi, A., and Bruce, R. 2001. CT-integrated robot for interventional procedures: Preliminary experiment and computer-human interfaces. *Computer Aided Surgery* 6(6):352–359.

Yen, P., Hibberd, R. D., and Davies, B. L. 1996. A telemanipulator system as an assistant and training tool for penetrating soft tissue. *Mechatronics* 6(4):423–436.